ADVANCED FUNCTIONAL MATERIALS
www.afm-journal.de

Hierarchical Composite Electrodes of Nickel Oxide Nanoflake 3D Graphene for High-Performance Pseudocapacitors

Chundong Wang, Junling Xu, Muk-Fung Yuen, Jie Zhang, Yangyang Li, Xianfeng Chen, and Wenjun Zhang**

NiO nanoflakes are created with a simple hydrothermal method on 3D (three-dimensional) graphene scaffolds grown on Ni foams by microwave plasma enhanced chemical vapor deposition (MPCVD). Such as-grown NiO-3D graphene hierarchical composites are then applied as monolithic electrodes for a pseudo-supercapacitor application without needing binders or metal-based current collectors. Electrochemical measurements impart that the hierarchical NiO-3D graphene composite delivers a high specific capacitance of ≈1829 F g^{-1} at a current density of 3 A g^{-1} (the theoretical capacitance of NiO is 2584 F g^{-1}). Furthermore, a full-cell is realized with an energy density of 138 Wh kg^{-1} at a power density of 5.25 kW kg^{-1}, which is much superior to commercial ones as well as reported devices in asymmetric capacitors of NiO. More attractively, this asymmetric supercapacitor exhibits capacitance retention of 85% after 5000 cycles relative to the initial value of the 1st cycle.

1. Introduction

With the depletion of traditional energy resources as well as the increasing energy demand, development of sustainable, clean energy-storage and delivery systems is an urgent task.[1–3] Fuel cells, secondary batteries, and capacitors are considered to be promising candidates for new energy systems to meet the requirement of high capacity, and fast charging/discharging rates. Among them, supercapacitors have attracted special attention because of their longer cycle life (up to 10^4 cycles), excellent safety, simple charging circuit, no memory effect, high power density and energy density.[3–6] Supercapacitors can be generally classified to two categories following the charge storage mechanism, of which they are electric double layer capacitors (EDLC) and pseudocapacitors. Because EDLC only store charges at the electrode and electrolyte interface, it provides a low energy density compared with their theoretical value, which dramatically limits their widely applications.[7,8] In contrast, pseudocapacitors deliver 3–4 times higher capacitance because the Faradic redox reaction happens not only on the surface, but also on the places near the surface of the active electrode.[8–10]

For making pseudocapacitors, the state-of-the-art material RuO_2 has been widely studied because of its great conductivity, reversible redox process, and high specific capacitance.[11,12] However, its practical application is impeded by the expensive and toxic nature. Thus, alternative metal oxides such as NiO, MoO_3, MnO_2, and Co_3O_4 have been suggested to be the potential candidates for supercapacitors.[10,13–15] Among them, NiO is one of the most promising materials due to its high theoretical capacitance of 2584 F g^{-1}, robust chemical/thermal stability, environment benign nature, low cost and easy preparation process.[16–19] However, the intrinsic high resistances of NiO (the electrical conductivity is less than 10^{-13} Ω^{-1} cm^{-1} at room temperature)[20] limits their charge/discharge rate, and power performance of electrode materials for high-power applications.[5,21,22] To solve this problem, various approaches have been proposed to design advanced supercapacitor electrodes with superior nanostructured NiO and well-defined electrode network to minimize the resistivity. For example, monolithic NiO/Ni nanocomposites delivered a specific capacitance of 900 F g^{-1} at 1 A g^{-1}.[17] With direct synthesis of porous NiO nanowall arrays on flexible Fe-Co-Ni conductive substrates, a specific capacitance of 270 F g^{-1} at a current density of 0.67 A g^{-1} was obtained.[23] By decorating NiO nanostructures on Ni foam-graphene,[24] graphene foam[25] and three dimensional graphene-Ni scaffold,[26] they exhibited increased electrochemical performances such as 783 F g^{-1} at 2 mV s^{-1}, 1225 F g^{-1} at 2 A g^{-1}, and 816 F g^{-1} at 5 mV s^{-1}, but all of the displayed specific capacitances are still far below the theoretical capacitance of NiO, which does not satisfy the demand in high powerful electronic devices.

In this work, we report a type of high-performance supercapacitor made from a hierarchical composite of nickel oxide nanoflakes on a 3D graphene architecture atop Ni foams. Different from the previously reported works,[26] herein, the graphene was 3D foothill-like instead of 2D film on 3D Ni foam.

Dr. C. D. Wang,[+] M.-F. Yuen, J. Zhang,
Prof. Y. Y. Li, Prof. X. F. Chen, Prof. W. J. Zhang
Center of Super-Diamond and
Advanced Films (COSDAF)
Department of Physics and Materials Science
City University of Hong Kong
Hong Kong SAR, China
E-mail: xianfeng.chen@cityu.edu.hk; apwjzh@cityu.edu.hk
J. L. Xu[+]
Department of Electronic Engineering
The Chinese University of Hong Kong
Hong Kong SAR, China
[+]C.D.W. and J.L.X. contributed equally to this work.

DOI: 10.1002/adfm.201401216

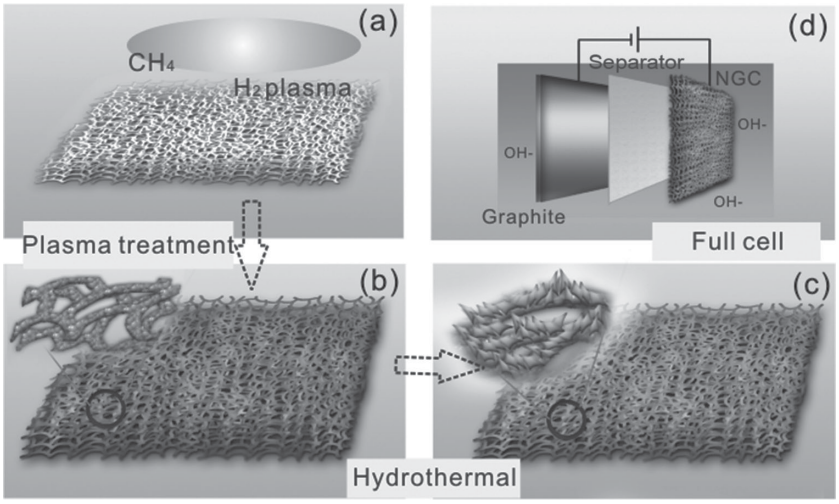

Scheme 1. Fabrication process of NiO-3D graphene composites (NGC) and the setup of using it for a full cell. a) Ni foam was treated with microwave plasma-enhanced CVD in a H_2/CH_4 mixture, b) the growth of 3D graphene architecture on the Ni foam, c) NGC was formed with hydrothermal synthesis in $NiCl_2$ solution, in which the NiO flakes were grown atop the 3D graphene scaffold, and d) the setup of a full cell composed of NGC, graphite (the counter electrode) and a separator in NaOH solution.

Therefore, the electrode has a hierarchical structure (**Scheme 1**). With this unique structure, our study shows that it can achieve a record high capacitance of 1421 F g^{-1} at a current density of 5 A g^{-1}. Furthermore, the resulting asymmetric pseudocapacitors exhibit an overall great performance of high capacitance, high energy density at high power density and long cycling life.

2. Results and Discussion

2.1. Synthesis and Structural Characterization

The schematic fabrication process of NiO nanoflake-3D graphene composite (NGC) preparation and the setup of an asymmetric pseudocapacitor (full cell) are shown in Scheme 1. The detailed illustration is described in the experimental section. The morphology and microstructure of the 3D graphene and NGC were examined by scanning electron microscopy (SEM) as shown in **Figure 1**. As depicted in Scheme 1a, Ni foam was used as a metal substrate for the synthesis of graphene. After growth of graphene in a MPCVD system, the color of the Ni foam changed from shiny white to light black as shown in Scheme 1. A magnified image is displayed in Figure 1a, from which the graphene sheets on the surface of Ni foam are observed. This is similar to our previously reported 3D graphene scaffold grown on Ni foils.[27,28] Herein, we use MPCVD system to treat with the Ni foam under CH_4/H_2 plasmas, by which 3D graphene was grown on the Ni foam scaffold instead of 2D graphene sheets. The reason for the formation of such a 3D graphene structure on the Ni foam in CH_4/H_2 plasmas is not yet well understood.[29,30] We assume that highly energetic reactive species (e.g., CH_x species, excited H atoms and ions) are generated in the plasmas, which is attributed to be the main reason for the direct growth of the 3D graphene on the Ni foam at high temperature. It is similar to the previously reported 3D graphene grown on stainless steel substrates[31] and Ni foils.[27,28] More detail information of the 3D graphene morphology were displayed in Figure S1 in the Supporting Information. After the aforementioned process, NiO nanoflakes were then grown on the surface of the 3D graphene by hydrothermal synthesis, the color changed to light blue as demonstrated in Scheme 1c. The SEM images of NGCs with different synthesis solution concentrations are exhibited in Figure 1b–f. Note that we added different amounts of nickel chloride (0.01, 0.05, 0.1, 0.3, and 0.5 g) with the same size of the 3D graphene-Ni foam in a 23 mL Teflon-lined stainless steel autoclave with 18 mL of deionized water. For simplicity, we define them as specimens of NGC-4 mM (NiO-3DG composite-4 mM), NGC-20 mM, NGC-40 mM, NGC-120 mM, and NGC-200 mM. In Figure 1b, thick flakes are observed for 4 mM of nickel chloride solution. Interestingly, when the Ni^+ solution concentration increases to 20 mM, the flakes become thinner (Figure 1c). However, the flakes were not grown up completely and uniformly. When the solution concentration increases to 40 mM, uniform and thin flakes with clear edges are revealed (Figure 1d). The length of the NiO flakes is about 1–2 μm with ultra-thin thickness. The uniform morphology cross a large area is verified with a low-magnification SEM image shown in the inset of **Figure 2**d. It is worth noting that a small difference in morphology may result in a large variation of electrochemical performance, which will be demonstrated in the aftermentioned text. With further increase of the solution concentration to 120 mM, the flakes become fat and grow along the face-direction (Figure 1e). As the solution concentration reaches 200 mM, a thick NiO thin film was formed on the top of the 3D graphene (Figure 1f). The inset SEM image of Figure 1f depicts that an irregular NiO thin film covers the whole surface of the 3D graphene without noticeable three-dimensional morphology. To understand the mechanism of the different morphologies of NiO, more experiments will be needed to carry out in the future work.

Raman spectroscopy was conducted for the 3D graphene and NiO-3D graphene composites (Figure 2a). Due to the best morphology of NGC-40 mM, it was chosen as the specimen. Three strong peaks of 3D graphene can be identified: i) the G band at ≈1576 cm^{-1}, assigned to the doubly degenerated E_{2g} mode of graphite, which is the characteristic peak of graphite;[32,33] ii) the symmetric 2D band at ≈2696 cm^{-1}, associated to the C–C sp^2 in-plane phonon vibrations, coming from two phonons with opposite momentum in the highest optical branch near the **K**;[34,35] iii) an explicit D peak (defect peak) at 1350 cm^{-1} was due to the defects in graphene.[36] It needs to point out that the 3D graphene may have more edges than 2D graphene sheets, and the graphene edges may also contribute to the D peak intensity. You et al.[37] reported that the intensity of D band is also correlated to the edge chirality: being stronger at the armchair edge and weaker at the zigzag edge. Since the peak intensity

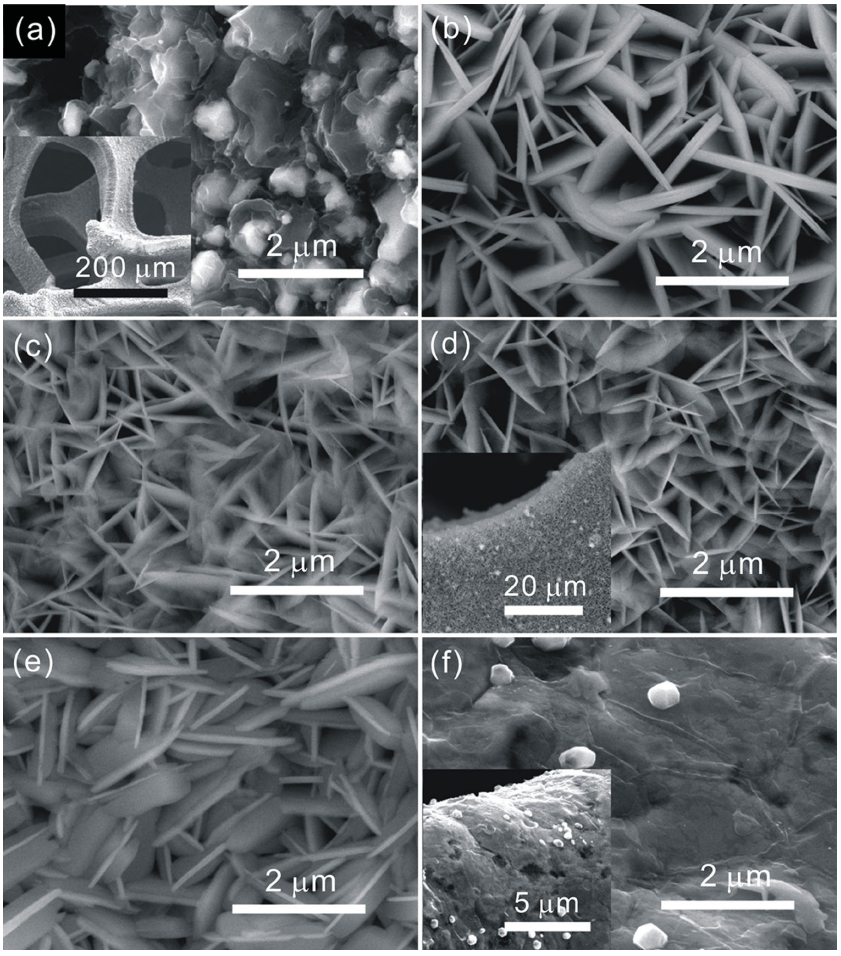

Figure 1. a) SEM image of 3D graphene grown on the surface of Ni foam. b–f) SEM images of NGC prepared in $NiCl_2$ solution of different concentrations (4, 20, 40, 120, and 200 mM). The samples are noted as b) NGC-4 mM, c) NGC-20 mM, d) NGC-40 mM, e) NGC-120 mM, and f) NGC-200 mM. The insets in (a,d,f) are the low-magnification images of 3D graphene on Ni foam, NGC-40 mM, and NGC-200 mM, respectively.

ratio of I_{2D}/I_G is less than 1, it is believed that the 3D graphene should be the stacking of multilayer graphene sheets, which is similar with those reported in our recent works.[27,28] The observations are consistent with those obtained on 3D graphene scaffold on Ni foils and single-graphene sheets grown from polymers on Cu under plasma.[27,28,32,35] In the Raman spectrum of NGC-40 mM, two more peaks appear accompanying with the D, G, 2D peaks of the 3D graphene. The sharp peak centered at 446 cm^{-1} is assigned to the first- phonon (1P) (TO and LO modes) scattering in NiO, while the broad peak in the range of 730–910 cm^{-1} is corresponding to the second- phonon (2P) (2TO and TO + LO modes) scattering in NiO.[25,38]

A typical TEM image of the NiO flake scraped from NGC-40 mM is shown in Figure 2b. The NiO flake has sharp edges and one edge length is about 1 μm, which is consistent with the SEM observation mentioned hereinbefore. The SAED pattern (inset of Figure 2b) reveals that it is polycrystalline with good crystallinity, of which it is corresponding to the (111), (200), (220), (311), and (222) planes of NiO. The high-resolution TEM image accompanying with a fast Fourier transform (FFT) pattern, demonstrating that the lattice spacing is 0.24 nm, which can be assigned to the (111) plane of NiO as shown in Figure 2d. Furthermore, the HRTEM image reflects that there should be many nanoporous holes on the surface of the NiO flake as the lattice unit was disturbed randomly, which is in line with the observations in Figure 2b,c. From Figure 2c (an enlarged TEM image of Figure 2b), it can be seen that the surface is rough, verifying the conclusion that the NiO flake should possess a porous structure.

2.2. Electrochemical Evaluation

To investigate the electrochemical behaviors of the NiO-3D graphene composite electrodes of different morphologies, cyclic voltammetry and galvanostatic charge–discharge techniques were applied. **Figure 3**a presents typical CV curves of bare 3D graphene and NGS electrodes in a 1 M NaOH electrolyte at a 50 mV s^{-1} scan rate between 0.0 and 0.6 V. Except the curve of the 3D graphene electrode, two strong redox peaks appeared in all other NiO-3D graphene composite electrodes. Basically, rectangular CV curves can be frequently seen in electrochemical double-layer capacitors. However, large redox current peaks can only be observed under Faradaic reaction. Thus, it can be deduced that the obtained capacitance is mainly derived from the surface Faradaic reaction, which can be expressed as[17]

$$NiO + OH^- \leftrightarrow NiOOH + e^- \quad (1)$$

In Figure 3a, symmetric redox peaks are demonstrated, indicating the reversibility of the electrodes. By comparison, it is found that the highest gravimetric current density can be obtained for NGC-40 mM. With the concentration of Ni^{2+} ion decreasing in the solution (hydrothermal synthesis solution), the current densities of NiO-3D graphene composite electrodes (NGC-4 mM and NGC-20 mM) decrease remarkably. In contrast, with increasing the concentrations of Ni^{2+} ion in the solution, the NiO flakes become "fat" and grow along the face direction of the flake. With the morphology change, the gravimetric current density starts to drop when the concentration is over 40 mM. Particularly, when the concentration of Ni^{2+} ion increases to 200 mM, a thick film covers on the 3D graphene. Correspondingly, the gravimetric current density decreases dramatically, similar with that of the bare 3D graphene as shown in Figure 3a. It suggests that the increased concentration leads to the enhanced NiO loading. Therefore, the intrinsic poor conductivity of metal oxides will restrict the efficient utilization of its capacitive performance. Thus, NGC-40 mM is found to be the optimal one for achieving outstanding performance supercapacitors because of its porous structure. In addition,

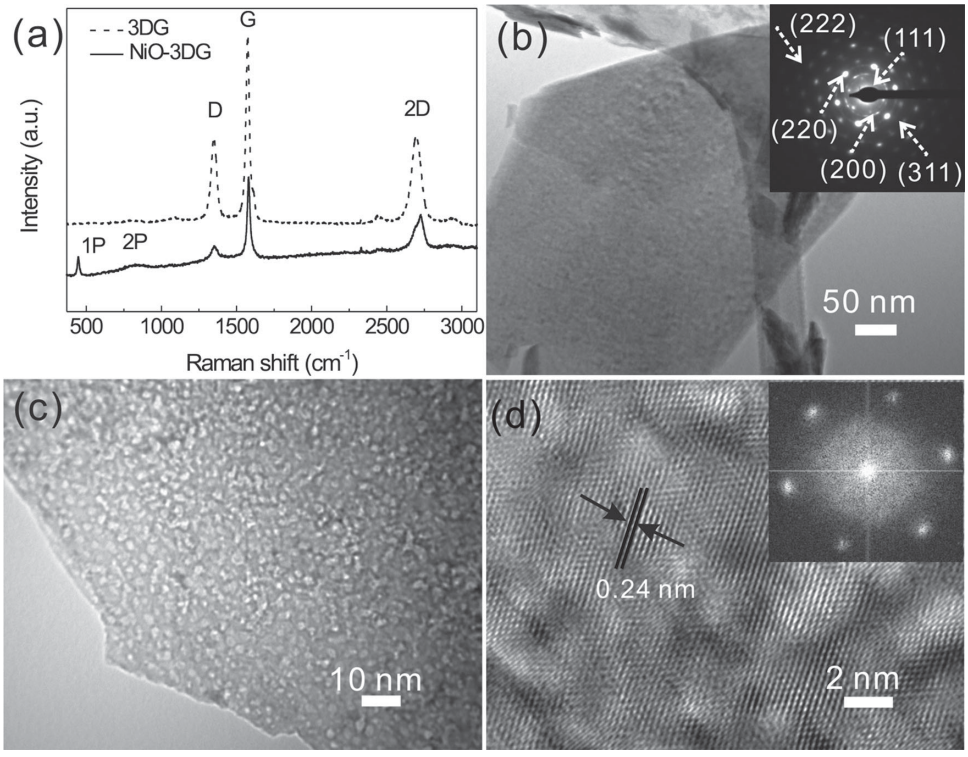

Figure 2. a) Raman spectra of 3D graphene and NGC-40 mM. b,c) TEM images of NiO flake with different magnifications. d) HRTEM image of NiO flake. The inset in (b) is the SAED pattern of NiO flake. The inset of (d) is the Fourier transform image of NiO flake.

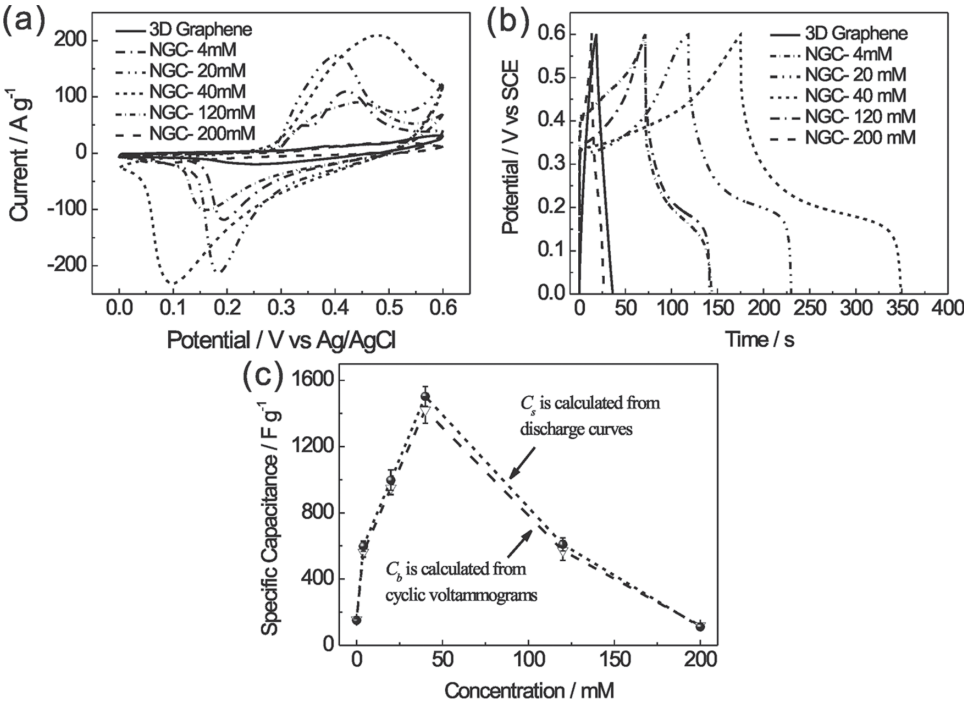

Figure 3. a) Cyclic voltammograms for bare 3D graphene electrodes and NiO-3D graphene composites at a scan rate of 50 mV s^{-1}. b) Charge–discharge curves at a current density of 5 A g^{-1}. c) Specific capacitance versus the concentrations of Ni^{2+} ion for NiO-3D graphene composites. Capacitance was estimated from the cyclic voltammograms at a scan rate of 50 mV s^{-1} and charge–discharge curves at a current density of 5 A g^{-1}.

we propose that the morphology and the crystallinity of the Ni flakes also play a key role in the electrochemical performance. As revealed in Figure 1, NGC-40 mM sample has an optimal morphology with uniformly and densely packed thin NiO flakes on the 3D graphene. In addition, the porous structure is considered as one of the important reasons for obtaining the outstanding-performance. To further evaluate the electrochemical performance and estimate its stable potential windows of the NiO-3D graphene composites, the galvanostatic charging/discharging was performed. Figure 3c presents nonlinear voltage–time profiles for the electrodes at a current density of 5 A g^{-1}, which are quite different from the general double-layer capacitors. The results indicate the happening of the Faradaic reactions, which is consistent with the above CV results.

The specific capacitance C (F g^{-1}), one of the most important parameters for characterizing the performance of capacitors, can be calculated from CV curves (C_b) and charge/discharge curves (C_s), respectively:

$$C_b = \frac{\int i\,dV}{\nu m V} \tag{2}$$

$$C_s = \frac{i\Delta t}{mV} \tag{3}$$

where i is the applied current (A), V the potential window (V), ν the scan rate (mV s^{-1}), Δt the discharge time (s), and m the mass (g) of the NiO-3D graphene composites. Based on the equations, C_b of the NiO-3D graphene composites are 563, 949, 1421, 572, and 118 F g^{-1} for NGC-4 mM, NGC-20 mM, NGC-40 mM, NGC-120 mM, and NGC-200 mM, respectively, at a scan rate of 50 mV s^{-1}. For the bare 3D graphene electrode, C_b is 154 F g^{-1}, comparable to the previously reported value (166 F g^{-1}) of the microwave exfoliated graphite oxide.[39] NGC-40 mM displays the highest C_s value (1503 F g^{-1}) among all of the NiO-3D graphene composites. It is notable that, although the NiO loading on the 3D graphene scaffold rises with the increase of the solution concentration, the specific capacitance does not achieve higher values for NGC-120 mM, and NGC-200 mM. Oppositely, when the NiO thick film covers the entire surface of the 3D graphene for NGC-200 mM, the lowest C_b (C_s), 118 F g^{-1} (120 F g^{-1}) is revealed. These phenomena are ascribed to the fact that the NiO thick film seals the surface of the 3D graphene, which effectively decreases the contact surface area between NiO and the electrolyte as well as reduces the conductivity of the electrode. These observations further verify the conclusion that the capacitance performance of the capacitors is highly dependent on the morphology of the NiO-3D graphene composites.

To investigate the capacity performance of NGC-40 mM, the effects of scan rates on the cyclic voltammogram and current density on the galvanostatic charge/discharge response of the electrodes were studied over a wide range as shown in **Figure 4**c. The specific capacitance decreases gradually with increased scan rates and current densities, due to a fact that electrolytic ions can diffuse and migrate into active materials

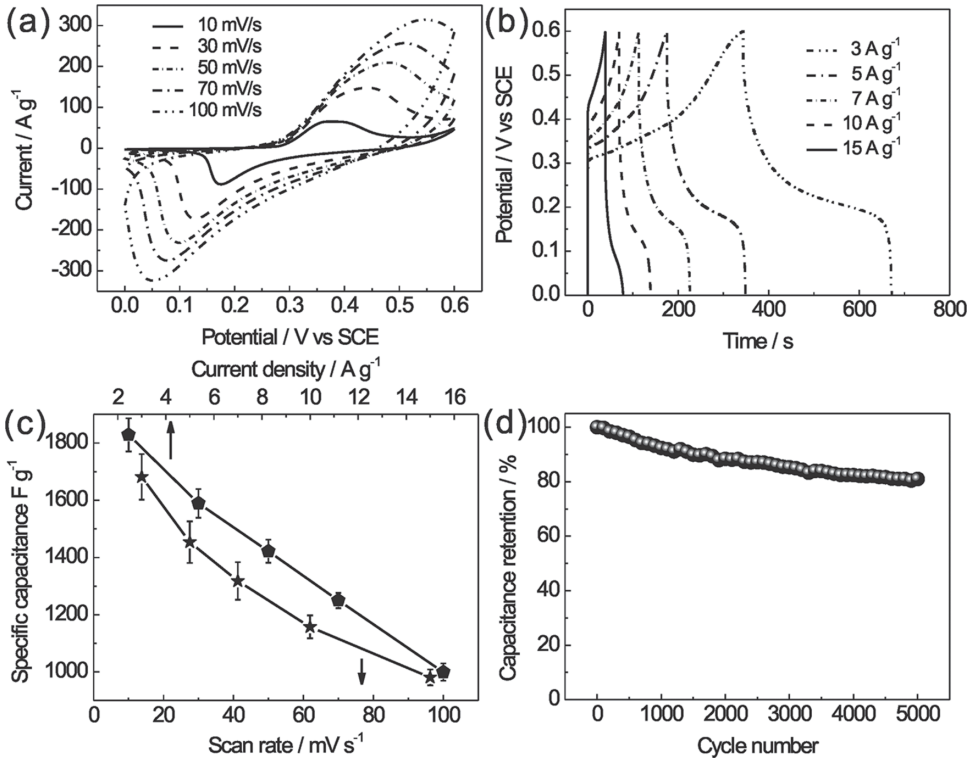

Figure 4. a) Cyclic voltammograms of NGC-40 mM at five different scan rates between 10 and 100 mV s^{-1} in 1 M NaOH. b) Charge–discharge curves at five current densities ranged between 3 and 15 A g^{-1}. c) Corresponding specific capacitance of NGC-40 mM versus scan rate and current density. d) Cycling stability of NGC-40 mM as a function of cycle number. The measurement of capacitance retention was carried out in the galvanostatic charge/discharge at a current density of 15 A g^{-1} for over 5000 cycles.

Table 1. Electrochemical performance of NiO-based Supercapacitors.

Specimen structure	Tested Current density [A g^{-1}/mA cm^{-2}]	Specific capacitance corresponding to the current density [F g^{-1}]	Cycling number	Capacity retention [%]	Year Published	Ref.
Porous NiO Nanocrystals	5 A g^{-1}	390	1000	–	2010	[45]
Porous NiO nanowall arrays on flexible Fe-Co-Ni alloy	0.67 A g^{-1}	270	4000	93	2011	[23]
NiO/graphene composites	1.4 A g^{-1}	745	2000	–	2011	[26]
Monlithic NiO/Ni nanocomposites	1 A g^{-1}	900	–	–	2011	[17]
Graphene sheet/porous NiO hybrid film	40 A g^{-1}	324	2000	94	2011	[43]
3D nanoporous NiO film	2.5 A g^{-1}	1790	1000	–	2012	[46]
NiO fine nanoparticles	0.275 A g^{-1}	243	–	–	2012	[40]
Nanoflower-shaped NiO	0.5 A g^{-1}	480	–	–	2012	[41]
NiO nanoflakes	0.5 mA cm^{-2}	401	500	92	2013	[47]
NiO nanostructures on Ni foam-graphene (NF-G/NiO)	–	783	1000	84	2013	[24]
Nano-architectured NiO/graphene foam	2 A g^{-1}	1225	–	–	2014	[25]
NiO/ultrathin derived graphene hybrid	10 A g^{-1}	300	500	90	2014	[44]
Nickel Oxide Nanoflake-3D grapheme Hierarchical composite (NGC)	3 A g^{-1}	1829	–	–	–	Present work
	15 A g^{-1}	980	5000	85%		

at a low scan rate and current density. In contrast, the restriction of diffusion and migration of electrolytic ions happens at a high scan rate and current density, leading to the inability of the inner active surface area for charge storage. The specific capacitances of NGC-40 mM were 1681, 1453,1318, 1157, and 981 F g^{-1} at scan rates of 10, 30, 50, 70, and 100 mV s^{-1}, as well as 1829, 1589, 1422, 1250, and 1000 F g^{-1} at current densities of 3, 5, 7, 10, and 15 A g^{-1}, respectively. For NiO nanostructures mixed with active carbon or acetylene black, the general specific capacitance is in the range of 200 to 400 F g^{-1}.[40,41] In a previous work, it was reported that monolithic NiO/Ni nanocomposite electrodes for electrochemical supercapacitors showed a remarkably high specific capacitance (ca. 900 F g^{-1}) because of the highly activated NiO surface layer and the conductive network of metal cores.[17] It is also noted that NiO/$Ni(OH)_2$ nanostructures obtained higher capacitance by connecting to graphene foam as well as 3D graphene architectures.[24–26,42] Furthermore, it was also observed that both two- and three-dimensional NiO could deliver more than 300 F g^{-1} specific capacitance at ultrahigh current densities (even up to 40 A g^{-1}) by combing with graphene to form hybrids, and the capacity retention can be nearly 90% after hundreds cycles.[43,44] For more detailed comparison of the electrochemical performance of the recent NiO-based Supercapacitors, it can refer to **Table 1**. Attractively, the delivered capacitance of the NGC in this work is the closest one to the theoretical value of NiO.[25] We speculate that the greatly enhanced performance is mainly due to the following reasons. i) The contact area between our 3D graphene and NiO nanoflakes in the unique hierarchical structure should significantly increase compared with the two dimensional graphene-NiO architectures (2D graphene on 3D Ni foam) found elsewhere,[26] which favors the charge transfer of the ions and electrons between the electrode and the current collector. ii) The 3D graphene architecture and highly porous NiO flakes can provide more active sites for electrochemical reactions which lead to faster kinetics in electrons and ions transportation. It is also confirmed that NGC-40 mM, which has the largest Brunauer-Emmett-Teller (BET) surface area of 227.7 m^2 g^{-1} (Figure S2, Supporting Information) among three samples, has the highest specific capacitance. iii) The formation of ultrathin NiO flakes (less than several nanometers) may probably facilitate the redox reaction. It was reported that the activation energy needed for oxidation and solid-state double decomposition reactions could be reduced with the decreased size of metal oxide and graphene/metal oxide nanostructures in lithium ion batteries.[48,49] iv) The as-prepared NiO/3D graphene composites grown on Ni foam were directly used as electrodes without any further treatment. Such a binder-free electrode dramatically increases conductivity, resulting in decreased contact resistance between the active materials and the current collectors when compared with those from general fabrication methods using polymeric binders. Figure 4d displays the relationship between the capacity retention and the cycling numbers of NGC-40 mM, which was tested at a current density of 15 A g^{-1} (the detail charge/discharge profile was given in the Supporting Information in Figure S3a). It is seen that it can maintain 81% of the initial capacitance after 5000 cycles, revealing excellent stability of the NiO-3D graphene composite electrodes.

To further evaluate the capacitive performance of the NiO-3D graphene composites in a full-cell, an asymmetric capacitor composed of NGC-40 mM (anode) and activated carbon (cathode) was setup (Scheme 1d). **Figure 5**a shows typical CV curves of the asymmetric capacitor tested in a 1 M NaOH electrolyte at various scan rates between 0 and 1.5 V. Two strong

redox peaks appear in each curve, which indicates that the pseudocapacitive activities of the asymmetric capacitor are induced by Faradaic reactions. Figure 5b presents the charge–discharge curves at various current densities. These curves display the nonlinearities between 0 and 1.5 V, which further confirms the Faradaic reaction happened in the asymmetric capacitor. Considering the total mass of the active materials (NGC-40mM and carbon) of the two electrodes, the electrochemical performance of the asymmetric cell vs various scan rates and current densities was conducted and the results are shown in Figure 5c. It reveals that the specific capacitances are 319, 210, 177, and 113 F g^{-1} at scan rates of 1, 3, 5, and 10 mV s^{-1}, as well as 440, 294, 171, and 130 F g^{-1} at current densities of 7, 10, 15, and 20 A g^{-1} in cyclic voltammetry curves and charge/discharge curves, respectively. Note that the specific capacitance of device is limited by the low capacity of cathode electrode.[50] Cycling galvanostatic charging and discharging of the asymmetric capacitor were further performed to evaluate the stability of the full-cell. The full-pseudocapacitors composed of the NiO-3D graphene composite and activated carbon depict excellent cycling performance as shown in Figure 5d. After 5000 cycles, the asymmetric full-capacitor experiences about 15% capacitance reduction. The increase of capacitance in the first 300 cycles was suggested to be attributed to the active process of the electrode.[51] For more detail charge/discharge profiles of 10 A g^{-1} and 15 A g^{-1}, it can be found in Figure S3 (Supporting Information). Energy density and power density are two important parameters that used for accessing the electrochemical performance of the capacitors. In the galvanostatic charge/discharge curves, the energy density (d_e) and power density (d_p) can be calculated using the equations as follows:

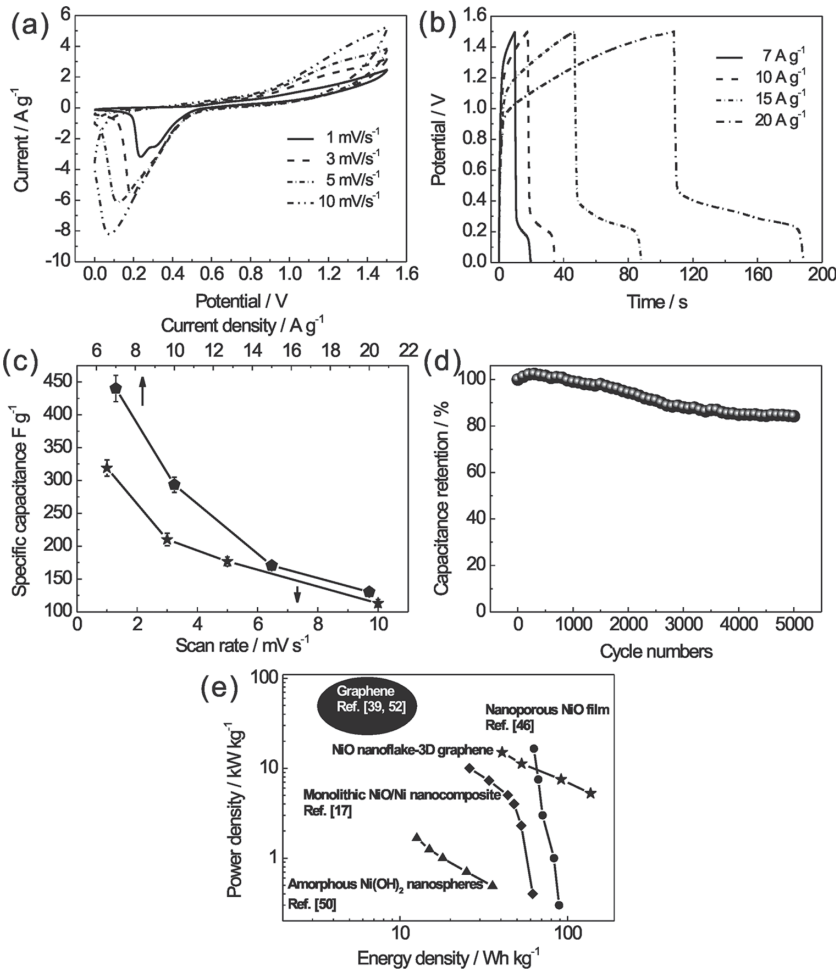

Figure 5. a) Cyclic voltammograms asymmetric capacitor composed of NGC-40 mM and activated carbon at various scan rates in 1 M NaOH. b) Charge–discharge curves of the capacitor at various current densities. c) Corresponding specific capacitance of the asymmetric capacitor versus scan rate and current density. d) Cycling stability of the asymmetric capacitor as a function of cycle number. The measurement of capacitance retention was performed in the galvanostatic charge/discharge at a current density of 10 A g^{-1} for over 5000 cycles. e) Ragone plot (energy density vs power density) of asymmetric capacitor composed of NGC-40 mM and activated carbon at different charge/discharge rates (the red curve), as well as other similar pseudocapacitors reported in the literature.[17,46,50] The black area is the capacitive performance of pure graphene reported in the literature.[39,52]

$$d_e = \frac{1}{2}CV^2 \quad (4)$$

$$d_p = \frac{d_e}{\Delta t} \quad (5)$$

Figure 5e depicts the Ragone plot (i.e., energy density vs power density). It shows that the maximum power density and the highest energy density of NiO-3D graphene composite electrode were 138 Wh kg^{-1} and 15 kW kg^{-1}, respectively. As redox reaction is the reason for the energy storage in pseudocapacitors, the energy densities of NiO or $Ni(OH)_2$ are larger than that of graphene, which stores energy by surface adsorption as highlighted in the black region in Figure 5e. However, because the redox reaction occurred on the surface or near the surface of NiO[17] or $Ni(OH)_2$,[46] which is relatively lower than the surface adsorption reaction happened in graphene-based double-layer capacitors, our pseudocapacitor demonstrates a little bit lower power density compared with other capacitor based on other materials (shown in Figure 5e). It is observed that both power density and energy density of amorphous $Ni(OH)_2$ are smaller than those of the other three pseudocapacitors based on NiO.[17,46,51] It needs to point out that although both the monolithic NiO/Ni nanocomposites and nanoporous NiO film possess high energy density and high power densities, however, it is tested in a single electrode, which is highly dependent on the discharge current density, and fluctuates dramatically with the energy densities. Here, in the NiO-3D graphene composites

full cell, we obtained an energy density of 138 Wh kg^{-1} at a power density of 5.25 kW kg^{-1}, which is extremely high for asymmetric capacitors. The resultant high power density, which is partially dependent on discharge densities, could be attributed to the well combination of 3D graphene with its enhanced porous structured NiO nanoflakes.

3. Conclusion

In this study, a novel approach is reported to synthesize hierarchical composite electrodes of nickel oxide nanoflake-three-dimensional graphene for high-performance pseudocapacitors. The device with optimum structure delivers a high specific capacitance of ≈1829 F g^{-1} at a current density of 3 A g^{-1}. In the asymmetric capacitor of using activated carbon as another electrode, an energy density of 138 Wh kg^{-1} can be achieved at a power density of 5.25 kW kg^{-1}, which is much higher than the commercially available asymmetric capacitors. After 5000 cycles, the asymmetric supercapacitor can still maintain 85% capacitance relative to the initial one. We believe that the binder-free nanoflake-structured NiO-graphene composites have promising outlook for high-performance supercapacitor applications.

4. Experimental Section

Material Synthesis: Nickel foam (Changsha Lyrun New Material Co., Ltd, China) with an area of 1 cm × 1 cm was washed in acetone, isopropyl alcohol, and deionized (DI) water. After dried with nitrogen gas, the Ni foam was subjected into a 1.5 kW ASTeX MPCVD system for the growth of 3D graphene on its surface. When the Ni foam was heated to 550 °C, which was measured by a thermal couple below the substrate holder, hydrogen plasma was produced using 1300 W microwave power. During the synthesis process, hydrogen and methane flow rates were 300 and 3 sccm, respectively, with a total pressure of 30 Torr. The synthesis duration was 30 min. After the plasma was switched off, the sample was cooled down to room temperature naturally. Nickel chloride (0.01, 0.05, 0.1, 0.3, and 0.5 g) and the 3D graphene-Ni foam were put in deionized water in a 23 mL Teflon-lined stainless steel autoclave containing 18 mL of deionized water. The sealed Teflon-lined autoclave was then placed into an oven at 200 °C for 13 h followed by natural cooling to room temperature. The synthesized NGC was washed with deionized water and alcohol for several times, and finally dried with nitrogen gas. For removing the Ni foam, the 3D graphene-Ni foam was placed in a polymethylmethacrylate (PMMA) solution (4% Sigma Aldrich No.182265 PMMA in Toluene). Then, the sample was removed from the solution and dried at 90 °C in an oven for 1 h. Subsequently, it was immersed in a mixture etchant solution of $FeCl_3$ (2 mol L^{-1}) and HCl (2 mol L^{-1}) at 60 °C until the Ni foam was completely removed. Finally, the PMMA coated 3D graphene was annealed in a MPCVD chamber at 700 °C in vacuum for 2 h to completely remove the PMMA with H_2 (200 sccm) and Ar_2 (100 sccm).

Characterization: The micro-structure of the as-prepared samples was characterized using scanning electron microscopy (SEM, Philips XL-30 FESEM), and transmission electron microscopy (TEM, JEOL TEM 2100F FEG operated with and accelerating voltage of 200 kV). Raman spectrum was conducted with a Renishaw-200 visual Raman microscope with a laser beam of 633 nm in wavelength at a spectral resolution of 1 cm^{-1} and spatial resolution of approximately 1 μm. The mass of 3D graphene and NiO nanoflakes were weighed 10 times by an electronic balance (Sartorius BP 211D) with a resolution of 0.01 mg and an average value was used. The values of the weight were obtained by calculating the mass difference before and after growth. NiO was weighed after annealing at 100 °C for 2 h to completely remove any residual solution. Taking Sample NGC-40 mm as an example, the mass of 3D graphene and NiO are 0.34 mg and 0.46 mg, respectively, and the mass of 3D graphene-NiO per area was calculated to be ≈0.8 mg cm^{-2}.

Electrochemical Measurements: The electrochemical measurements for single electrodes were recorded in a three-electrode electrochemical cell with a Pt counter electrode and a saturated calomel reference electrode (SCE) in a 1 M NaOH solution. The area ratio between Pt counter electrode and working electrode is 1:1. The electrochemical measurements for pseudocapacitors were carried out using a two-electrode configuration in a 1 M NaOH solution. The NiO-3D graphene composite electrodes were used as the working electrodes. Cyclic voltammetry and galvanostatic charge/discharge tests were used to characterize the electrochemical behavior of the single electrode and pseudocapacitors. The cycling stabilities of three-electrode cells and full cells were carried out under constant current densities, that is, 15 A g^{-1} for three-electrode cells and 10 A g^{-1} for full cells for over 5000 cycles.

Supporting Information

Supporting Information is available from the Wiley Online Library or from the author.

Acknowledgements

C. D. Wang is grateful to Z. Y. Zhang, Department of Physics and Materials Science, City University of Hong Kong, for his effort in drawing the schematic diagram. This work was supported by National Natural Science Foundation of China (NSFC Grant 61176007 and 51372213) and Research Grants Council of the Hong Kong Special Administrative Region, China (Project No. CityU 104911).

Received: April 16, 2014
Revised: May 26, 2014
Published online: August 14, 2014

[1] D. V. Esposito, S. T. Hunt, A. L. Stottlemyer, K. D. Dobson, B. E. McCandless, R. W. Birkmire, J. G. Chen, *Angew. Chem. Int. Ed.* **2010**, *49*, 9859.
[2] A. S. Aric, P. Bruce, B. Scrosati, J. M. Tarascon, W. Van Schalkwijk, *Nat. Mater.* **2005**, *4*, 366.
[3] P. Simon, Y. Gogotsi, *Nat. Mater.* **2008**, *7*, 845.
[4] P. J. Hall, M. Mirzaeian, S. I. Fletcher, F. B. Sillars, A. J. R. Rennie, G. O. Shitta-bey, G. Wilson, A. Cruden, R. Carter, *Energy Environ. Sci.* **2010**, *3*, 1238.
[5] H. Wang, H. S. Casalongue, Y. Liang, H. Dai, *J. Am. Chem. Soc.* **2010**, *132*, 7472.
[6] G. Yu, L. Hu, N. Liu, H. Wang, M. Vosgueritchian, Y. Yang, Y. Cui, Z. Bao, *Nano Lett.* **2011**, *11*, 4438.
[7] K. H. An, W. S. Kim, Y. S. Park, J. M. Moon, D. J. Bae, S. C. Lim, Y. S. Lee, Y. H. Lee, *Adv. Funct. Mater.* **2001**, *11*, 387.
[8] A. K. Shukla, S. Sampath, K. Vijayamohan, *Curr. Sci.* **2000**, *79*, 1656.
[9] H. Jiang, C. Z. Li, T. Sun, J. Ma, *Nanoscale* **2012**, *4*, 807.
[10] X. H. Xia, J. P. Tu, X. L. Wang, C. D. Gu, X. B. Zhao, *J. Mater. Chem.* **2011**, *21*, 671.
[11] C. CHu, K. H. Chang, M. C. Lin, Y. T. Wu, *Nano Lett.* **2006**, *6*, 2690.
[12] R. Vellacheri, V. K. Pillai, S. Kurungot, *Nanoscale* **2012**, *4*, 890.
[13] T. Brezesinski, J. Wang, S. H. Tolbert, B. Dunn, *Nat. Mater.* **2010**, *9*, 146.
[14] J. Zhu, J. He, *ACS Appl. Mater. Interfaces* **2012**, *4*, 1770.

[15] H. Cheng, Z. G. Lu, J. Q. Deng, C. Y. Chung, K. Zhang, Y. Y. Li, *Nano Res.* **2010**, *3*, 895.
[16] K. C. Liu, M. A. Anderson, *J. Electrochem. Soc.* **1996**, *143*, 124.
[17] Q. Lu, M. W. Lattanzi, Y. Chen, X. Kou, W. Li, X. Fan, K. M. Unruh, J. G. Chen, J. Q. Xiao, *Angew. Chem. Int. Ed.* **2011**, *50*, 6847.
[18] K. W. Nam, K. B. Kim, *Electrochem. Soc.* **2002**, *149*, 346.
[19] F. Luan, G. Wang, Y. Ling, X. Lu, H. Wang, Y. Li, *Nanoscale* **2013**, *5*, 7984.
[20] V. Biju, M. Abdul Khadar, *J. Mater. Sci.* **2001**, *36*, 5779.
[21] W. Sugimoto, H. Iwata, Y. Yasunaga, Y. Murakami, Y. Takasu, *Angew. Chem. Int. Ed.* **2003**, *42*, 4092.
[22] L. Zhang, F. Zhang, X. Yang, G. Long, Y. Wu, T. Zhang, K. Leng, Y. Huang, Y. Ma, A. Yu, Y. Chen, *Sci. Rep.* **2013**, *3*, 1408.
[23] J. Zhu, J. Jiang, J. Liu, R. Ding, H. Ding, Y. Feng, G. Wei, X. Huang, *J Solid State Chem.* **2011**, *184*, 578.
[24] A. Bello, K. Makgopa, M. Fabiane, D. Dodoo-Ahrin, K. I. Ozoemena, N. Manyala, *J Mater. Sci.* **2013**, *48*, 6707.
[25] H. Wang, H. Yi, X. Chen, X. Wang, *J. Mater. Chem. A* **2014**, *2*, 3223.
[26] X. Cao, Y. Shi, W. Shi, G. Lu, X. Huang, Q. Yan, Q. Zhang, H. Zhang, *Small* **2011**, *7*, 3163.
[27] C. D. Wang, Y. Li, Y. S. Chui, Q. H. Wu, X. F. Chen, W. J. Zhang, *Nanoscale* **2013**, *5*, 10599.
[28] C. D. Wang, Y. S. Chui, R. G. Ma, T. L. Wong, J. G. Ren, Q. H. Wu, X. F. Chen, W. J. Zhang, *J. Mater. Chem. A* **2013**, *1*, 10092.
[29] N. G. Shang, P. Papakonstantinou, M. McMullan, M. Chu, A. Stamboulis, A. Potenza, S. S. Dhesi, H. Marchetto, *Adv. Funct. Mater.* **2008**, *18*, 3506.
[30] T. Bhuvana, A. Kumar, A. Sood, R. H. Gerzeski, J. Hu, V. S. Bhadram, C. Narayana, T. S. Fisher, *ACS Appl. Mater. Interfaces* **2010**, *2*, 644.
[31] A. Malesevic, R. Vitchev, K. Schouteden, A. Volodin, L. Zhang, G. V. Tendeloo, A. Vanhulsel, C. Van Haesendonck, *Nanotechnology* **2008**, *19*, 305604.
[32] C. D. Wang, M. F. Yuen, T. W. Ng, S. K. Jha, Z. Z. Lu, S. Y. Kwok, T. L. Wong, X. Yang, C. S. Lee, S. T. Lee, W. J. Zhang, *Appl. Phys. Lett* **2012**, *100*, 253107.
[33] W. Qian, X. Cui, R. Hao, Y. L. Hou, Z. Y. Zhang, *ACS Appl. Mater. Interfaces* **2011**, *3*, 2259.
[34] A. C. Ferrari, J. C. Meyer, V. Scardaci, C. Casiraghi, M. Lazzeri, F. Mauri, S. Piscanec, D. Jiang, K. S. Novoselov, S. Roth, A. K. Geim, *Phys. Rev. Lett.* **2006**, *97*, 187401.
[35] C. D. Wang, Y. G. Zhou, L. F. He, T. W. Ng, G. Hong, Q. H. Wu, F. Gao, C. S. Lee, W. J. Zhang, *Nanoscale* **2013**, *5*, 600.
[36] L. G. Cancado, A. Jorio, E. H. M. Ferreira, F. Stavale, C. A. Achete, R. B. Capaz, M. V. O. Moutinho, A. Lombardo, T. S. Kulmala, A. C. Ferrari, *Nano Lett.* **2011**, *11*, 3190.
[37] Y. You, Z. Ni, T. Yu, Z. Shen, *Appl. Phys. Lett.* **2008**, *93*, 163112.
[38] N. Mironova-Ulmane, A. Kuzmin, I. Steins, J. Grabis, I. Sildos, M. Pärs, *J. Phys. Conference Series* **2007**, *93*, 012039.
[39] Y. Zhu, S. Murali, M. D. Stoller, K. J. Ganesh, W. Cai, P. J. Ferreira, A. Pirkle, R. M. Wallace, K. A. Cychosz, M. Thommes, D. Su, E. A. Stach, R. S. Ruoff, *Science* **2011**, *332*, 1537.
[40] M. P. Yeager, D. Su, N. S. Marinkovi , X. Teng, *J. Electrochem. Soc.* **2012**, *159*, A1598.
[41] S. I. Kim, J. S. Lee, H. J. Ahn, H. K. Song, J. H. Jang, *ACS Appl. Mater. Interfaces* **2013**, *5*, 1596.
[42] J. Ji, L. L. Zhang, H. Ji, Y. Li, X. Zhao, X. Bai, X. Fan, F. Zhang, R. S. Ruoff, *ACS Nano* **2013**, *7*, 6237.
[43] X. Xia, J. Tu, Y. Mai, R. Chen, X. Wang, C. Gu, X. Zhao, *Chem. Eur. J.* **2011**, *17*, 10898.
[44] C. Wu, S. Deng, H. Wang, Y. Sun, J. Liu, H. Yan, *ACS Appl. Mater. Interfaces* **2014**, *6*, 1106.
[45] X. Zhang, W. Shi, J. Zhu, W. Zhao, J. Ma, S. Mhaisalkar, T. L. Maria, Y. Yang, H. Zhang, H. H. Hng, Q. Yan, *Nano Res.* **2010**, *3*, 643.
[46] K. Liang, X. Tang, W. Hu, *J. Mater. Chem.* **2012**, *22*, 11062.
[47] S. Vijayakumar, S. Nagamuthu, G. Muralidharan, *ACS Appl. Mater. Interfaces* **2013**, *5*, 2188.
[48] P. L. Taberna, S. Mitra, P. Poizot, P. Simon, J. M. Tarascon, *Nat. Mater.* **2006**, *5*, 567.
[49] D. Wang, J. Yang, X. Li, D. Geng, R. Li, M. Cai, T. K. Sham, X. Sun, *Energy Environ. Sci.* **2013**, *6*, 2900.
[50] H. B. Li, M. H. Yu, F. X. Wang, P. Liu, Y. Liang, J. Xiao, C. X. Wang, Y. X. Tong, G. W. Yang, *Nat. Commun.* **2013**, *4*, 1894.
[51] X. Lu, D. Zheng, T. Zhai, Z. Liu, Y. Huang, S. Xie, Y. Tong, *Energy Environ. Sci.* **2011**, *4*, 2915.
[52] X. Yang, C. Cheng, Y. Wang, L. Qiu, D. Li, *Science* **2013**, *341*, 534.